International Journal of Solids and Structures 309 (2025) 113175

Contents lists available at ScienceDirect

International Journal of Solids and Structures

journal homepage: www.elsevier.com/locate/ijsolstr

Inverse design of short-range order arrangement via neural network

Daegun You [a], Orcun Koray Celebi [a,b], Diab W. Abueidda [c,d], Gorkem Gengor [a], Ahmed Sameer Khan Mohammed [a], Seid Koric [a,c], Huseyin Sehitoglu [a,*]

[a] Department of Mechanical Science and Engineering, University of Illinois at Urbana-Champaign, 1206 W. Green St, Urbana, IL 61801, USA
[b] Department of Mechanical Engineering, Bilkent University, Ankara 06800, Turkey
[c] National Center for Supercomputing Applications, University of Illinois at Urbana-Champaign, 1205W. Clark St, IL 61801, USA
[d] Civil and Urban Engineering Department, New York University Abu Dhabi, United Arab Emirates

ARTICLE INFO

Keywords:
Machine learning
Short-range order
Monte Carlo
Stacking fault
Critical stress

ABSTRACT

Short-range order (SRO) plays a critical role in the mechanical behavior of metallic alloys. The arrangement of atoms at short ranges significantly impacts how the material responds to external forces. Nevertheless, the mechanics of these phenomena remain poorly understood. The identification of SRO in experiments is constrained by the low resolution of intensity distribution and the limitations associated with the direct observation of atomic arrangements in the lattice within the SRO domains. On the other hand, modeling the mechanical properties of short-range-ordered alloys is challenged by computationally expensive density functional theory (DFT)-based Monte Carlo (MC) simulations required to achieve the SRO structure dictated by energy minimization. This study aims to replace these expensive simulations with a trained machine learning (ML) model that yields accurate energy values for a given atomic structure. Further, we train an inverse model to determine the atomic configuration corresponding to the given SRO parameter. We propose a data-driven approach to map out the SRO directly to the atomic arrangements, combining ab initio calculations and a Neural Network (NN) model. We perform DFT-based MC simulations for Ni-V alloys in a wide range of solute compositions. Then, forward and inverse NN models are trained to map the SRO parameters into atomic arrangements or vice-versa. We predict the critical resolved shear stress (CRSS) for slip for all the studied configurations encompassing random and SRO structures and discuss the effect of SRO on the flow stress. The proposed ML methodology provides atomic arrangements from target order parameters with high accuracy, thereby eliminating the need for expensive simulations, and it advances the understanding of SRO at the atomistic scale.

1. Introduction

The critical resolved shear stress (CRSS) is a fundamental quantity in materials science and mechanics that governs mechanical behavior (Abuzaid and Sehitoglu, 2017; Argon, 2007; Asaro and Lubarda, 2006; Celebi et al., 2023; Nabarro, 1947; Peierls, 1940; Schoeck, 1994; You et al., 2024; You et al., 2023a; You et al., 2023b). It is the backbone of crystal plasticity calculations, strain localization, fracture and fatigue studies, and strongly depends on the composition. The CRSS determination without empiricism has been challenging because it depends on many factors including the fault energies, the elastic energies, and the specific crystal lattice type. The total energies, when minimized, give a measure of the CRSS. However, the total energy calculation is contingent on the initial atomic positions of the species. Once these atomic positions are established, the statistical variation of the fault energies can be assessed on different slip cuts to provide a range of CRSS values. Even for a binary alloy, determining the atomic positions requires lengthy simulations involving atom swapping with thousands of iterations. This study aims to find a methodology to accelerate these calculations, ultimately obtaining the minimum energy configurations. The work will ultimately be of direct benefit to the development of advanced metallic alloys, as described below.

Advanced materials such as compositionally complex alloys renewed interest in chemical short-range order (SRO) effects, which can affect the energy barriers for slip, CRSS calculations, and other physical properties. Chemical SRO, which refers to the localized preferential bonding of specific atom types, can manifest in alloys that lack long-range order and exhibit overall disorder. Its impact on the mechanical properties of alloys is widely recognized (Chen et al., 2021a; Chen et al., 2021b; Ding et al., 2018; Li et al., 2019; Niu et al., 2018; Picak et al., 2023; You et al.,

* Corresponding author.
E-mail address: huseyin@illinois.edu (H. Sehitoglu).

https://doi.org/10.1016/j.ijsolstr.2024.113175
Received 28 May 2024; Received in revised form 10 November 2024; Accepted 28 November 2024
Available online 29 November 2024

2024; Zhang et al., 2022; Zhang et al., 2020; Zhang et al., 2019; Zhao et al., 2019; Zhao et al., 2017; Zhou et al., 2022). While SRO has been extensively examined using diffuse scattering methods, these techniques are constrained by low resolution to characterize the exact local atomic configuration (Chen et al., 2021b; Picak et al., 2023; Zhang et al., 2022; Zhang et al., 2020; Zhang et al., 2019; Zhou et al., 2022). Although alternative experimental approaches, such as atomic probe tomography, can offer insights into the local environment of alloys at the atomic scale (Li et al., 2023; Marceau et al., 2015a; Marceau et al., 2015b; Pradeep et al., 2013), they suffer from high costs and time-consuming procedures. This paper focuses on an accelerated computational model based on atomistic simulations, aiming to elucidate the determination of SRO, local configurations, and their effect on the mechanical behavior of alloys.

A commonly used computational approach to study SRO is Monte Carlo (MC) simulation combined with molecular dynamics (MD) or ab initio calculations such as density functional theory (DFT) (Chen et al., 2021a; Ding et al., 2018; Ferrari et al., 2023; Li et al., 2019; You et al., 2024). Additionally, in order to get the SRO structures, hybrid calculations combining empirical potentials are implemented to accelerate the MC simulation (Widom et al., 2014; You et al., 2024), but each step still requires to perform a DFT-based calculation. This leads to hundreds of computationally expensive DFT simulations to obtain the targeted lower energy configuration. Due to the high computational cost in the MC simulation, the cluster expansion theory is occasionally employed to support the calculations to estimate the total energy of atomistic configuration (Chen et al., 2021b). However, it suffers from a narrow compositional range and a small number of elements since it interpolates total energy utilizing the provided data for the specific alloy system. Also, this methodology is unable to produce the exact atomistic configurations from the material properties.

Recent years have seen a rapid advancement in machine learning (ML) techniques, which have led to a wide range of applications in industries such as bioinformatics, autonomous driving, image and speech recognition, medical diagnostics, and bio-inspired design, among many others. The ML techniques have lately been used to design and characterize materials on all scales, such as in topological optimization in *meta*-materials (Kollmann et al., 2020), crystal plasticity characterization on a micro-scale (Muhammad et al., 2021; Salmenjoki et al., 2018), thermo-viscoplasticity (Abueidda et al., 2021), and characterization of charge-density fields to evaluate the elastic moduli (Barry et al., 2023). At the lattice level, the ML models were trained with limited data from computationally expensive DFT calculations to instantly infer point defect in crystal (You et al., 2020), and inter-atomic potentials in MD simulations (Santos-Florez et al., 2023; Wang et al., 2022; Yin et al., 2021), promoting significant computation efficiencies with exceptional accuracy.

However, to the author's best knowledge, there are no studies that achieved both forward modeling of SRO and its inverse design, i.e., not only to predict SRO but also for the given desired SRO infer the underlying atomic configuration. In addition, the high-throughput and parallel capabilities of modern high-performance computing systems enabled the generation of enough high-fidelity training data from DFT-based MC simulations, avoiding compromising accuracy, such as with classical or ML-based potentials in MD simulations. In this study, we propose a ML approach to accelerate the MC simulation and map out atomistic configuration via the corresponding SRO parameters. The workflow diagram of the present study is shown in Fig. 1, which is elaborated below.

The first step involves acquiring datasets, which do not require ML. We utilize a DFT-based MC simulation to gather the necessary data for FCC Ni-V alloys across a broad spectrum of solute compositions, ranging from 5 at.% to 36.3 at.% V. The random configurations are initially set in the DFT-MC simulation for all the studied compositions. The DFT-MC simulation is implemented over 10 steps to obtain the training dataset, with each step taking 40 min (t_{cpu}) on multi-cores CPU. Following this, the forward neural network (*f-NN*) model is trained to accelerate the MC simulation, enabling the minimum energy structure to be obtained almost instantly ($t_{cpu} \sim 1$ ms). In the *f-NN* model, the features include atomic species and coordinates, while the design variable is the total energy of the configuration. The second ML model is the inverse neural network (*i-NN*), which generates atomic configurations directly from SRO parameters, bypassing the need for MC simulation. In the *i-NN* model, the features are the SRO parameters, and the design variables are the atomic species and coordinates. Here, by using "SRO change" theory to the *i-NN*-generated atomic configurations allows for the instant

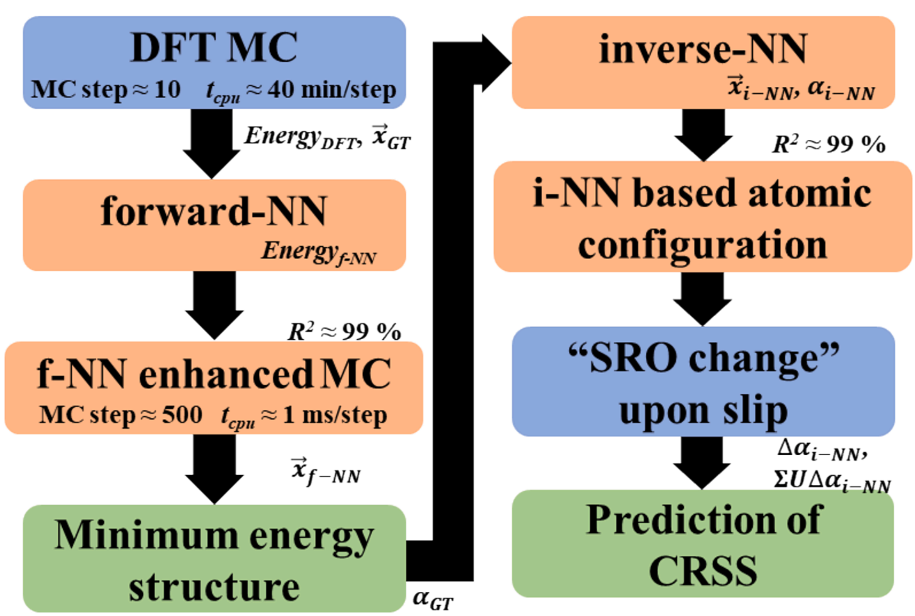

Fig. 1. Flowchart of machine learning (ML) based prediction of short-range order (SRO) configuration and critical resolved shear stress (CRSS); Forward and inverse neural network (*f-NN*, *i-NN*) models are developed for two different design variables; Input and theoretical calculations are colored blue, the ML training and test are orange, and output and targets of models are green, respectively; $\vec{x}_{GT}$, $\vec{x}_{f-NN}$ and $\vec{x}_{i-NN}$ are ground truth (GT), *f-NN*, and *i-NN* based coordinates of atomic configurations. α_{GT}, α_{i-NN}, $\Delta\alpha_{i-NN}$, and $\Sigma U\Delta\alpha_{i-NN}$ are GT, *i-NN* based SRO, "SRO change", and summation of "SRO change" weighted by interaction energy.

prediction of the CRSS, the targeted mechanical property. The proposed methodology, utilizing the NN models, yields the targeted SRO configurations with high accuracy, eliminating the need for expensive DFT-MC simulations and contributing to the understanding of SRO at the atomistic scale. We expect the current model to facilitate the design of SRO in materials toward desirable mechanical properties by users.

2. Methods

2.1. Monte Carlo simulation based on DFT

In order to obtain SRO structures, we implement MC simulations of swapping atomic species, and each step performs a DFT-based calculation. We employ the Vienna Ab initio Simulation Package (VASP) for the DFT simulations (Kresse and Furthmüller, 1996). First, we create an FCC Ni superlattice containing 270 atoms with 9 stacking layers of {1 1 1} plane. Ni atoms are substituted with V atoms corresponding to the targeted composition. Then, the MC simulation of swapping atomic species (Ni and V) is carried out based on the Metropolis-Hasting criterion (Hastings, 1970). The candidate configuration is accepted: 1) if the energy of swapped configuration E(i + 1) is lower than the previous one E (i), or 2) the following probability is equal to / greater than the random number (R) ranged by (0, 1),

$$R \leq \exp\left(-\frac{E(i+1)-E(i)}{kT_s}\right) \tag{1}$$

where k is Boltzmann constant, and T_s is a temperature-scaling factor. The T_s is set to 10 K for most compositions, except the two configurations (300 K, 500 K) in $Ni_{63.7}V_{36.3}$ composition for a structural variety with higher thermal assistance. At each MC step, 10 random swaps of Ni and V atoms are performed, and the resulting configuration is accepted if the above conditions are met.

The DFT calculations are implemented within the projected-augmented-waves (PAW) (Kresse and Joubert, 1999) approach via Perdew-Burke-Ernzerhof (PBE) (Perdew et al., 1996) exchange–correlation potentials. The PAW-PBE pseudopotentials for V and Ni are employed with the following valence electron configurations V (3 s^2, 3p^6, 3d^4, 4 s^1) and Ni (3p^6, 3d^9, 4 s^1), respectively. The oriented FCC superlattice with 270 atoms is employed with Monkhorst-pack k-mesh 1 × 1 × 1 for the MC simulations of swapping atoms. A 450 eV plane-wave energy cut-off is used for all the calculations. The tolerance criteria for energy and force are allowed within 1 meV and 5 meV/Å, respectively. High-throughput computing on the Delta high-performance computing system at the National Center for Supercomputing Applications (NCSA) is leveraged to run several independent DFT-MC simulation instances simultaneously, each running on a separate computing node using parallel VASP features on its multi-core CPU cores. This setup allowed the relatively quick generation of high-fidelity training and testing data from the first principle within a week.

2.2. Short-range order characterization

At each MC simulation step, we calculate the total energy and Warren-Cowley (WC) based SRO parameters (Cowley, 1960; Norman and Warren, 2004). The SRO parameters are defined at different nearest neighbor shells surrounding the host atom. The SRO parameter is expressed as follows:

$$\alpha_{i-j}^{m} = 1 - \frac{p_{i-j}^{m}}{c_j} \tag{2}$$

where p_{i-j}^{m} is the probability of finding an atomic species (j) around the host (i) in m-th neighbor shell, and c_j is the concentration of atomic species (j). In the main text, we focus on the SRO parameter for the first shell since it dominantly contributes to the SRO (You et al., 2024). We obtain a total of 2,125 distinct SRO configurations (including random, intermediate, and final structures) for different vanadium concentrations (5, 10, 15, 20, 25, 30, and 36.3 at. %) of Ni-V alloys. The random configurations, i.e. those with SRO parameters closest to zero, are obtained using the ATAT package (van de Walle et al., 2013).

2.3. Neural network modeling

We employ a ML model that utilizes a neural network (NN) algorithm for predicting both the total energy and atomic configurations. Fig. 2 shows a deep feedforward NN made up of interconnected layers of neurons. The network takes an input layer $\boldsymbol{X}$ (possessing p features) and computes an output layer $\boldsymbol{Y}$ (possessing q targets). The depth of a NN is determined by the number of hidden layers, which are the layers between the output and input layers. Each neuron within these layers possesses weights $\boldsymbol{W}$, biases $\boldsymbol{b}$, and activation functions f, facilitating the calculation of the numeric flow in the subsequent layer. Subsequently, all hidden layers and the output layer iteratively perform calculations in the forward direction:

$$\begin{aligned} \boldsymbol{Z}^l &= \boldsymbol{W}^l\boldsymbol{Y}^{l-1} + \boldsymbol{b}^l \\ \boldsymbol{Y}^l &= f(\boldsymbol{Z}^l) \end{aligned} \tag{3}$$

where the weights $\boldsymbol{W}$ and biases $\boldsymbol{b}$ are updated after every training (optimization) iteration. The activation function f^l is a mapping from $\mathbb{R}\rightarrow\mathbb{R}$ that transforms the vector $\boldsymbol{Z}^l$, calculated using weights and biases, into the output for each neuron in layer l.

In each epoch, the output layer computes a loss (error) between the prediction and ground truth for the target, such as total energy or atomic configuration. Based on this loss, all layers adjust the weights and biases between their neurons through back-propagation. This training (optimization) process of forward and back-propagation is repeated throughout the total number of epochs. One of the most common and most straightforward optimizers used is gradient descent (Pattanayak et al., 2017):

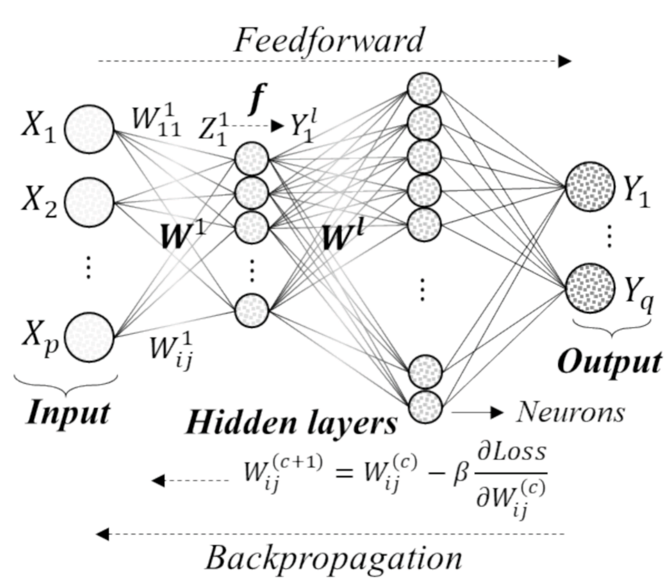

Fig. 2. Schematic of a fully connected (dense) artificial neural network (NN) with p features (X_p) and q outputs (Y_q). Dashed arrows are feedforward or backpropagation of updating weight tensors (W_{ij}^l) of l-layer at c iteration. The activation function (f) transforms the vector Z to the intermediate and final outputs Y.

$$W_{ij}^{(c+1)} = W_{ij}^{(c)} - \beta \frac{\partial Loss}{\partial W_{ij}^{(c)}}$$
$$b_i^{(c+1)} = b_i^{(c)} - \beta \frac{\partial Loss}{\partial b_i^{(c)}} \tag{4}$$

where β is the learning rate. Eq. (4) shows how the weights and biases at a given iteration c within the gradient descent training process are updated. The gradient term of the loss function can be modified depending on the choice of optimizer in the NN modeling, which helps the model to avoid potential local minima and overfitting. Details of optimizer algorithms can be found elsewhere (Goodfellow, 2016). In both *f-NN* and *i-NN* models, we used Adaptive moment estimation (Adam) optimizer, which dynamically adjusts the β parameters based on the individual weights of the neurons.

In this study, we utilize NN models for two purposes: 1) predicting the total energy from the atomic configuration to accelerate energy calculations for the MC algorithm, and 2) determining the atomic configuration based on SRO parameters for the inverse design of materials. Both forward and inverse NN models are trained using a dataset of 2,125 atomic configurations with varying solute compositions and SRO parameters. The two ML models are implemented and trained using the PyTorch library. The dataset was split into an 80/20 ratio for training and testing, respectively.

2.3.1. Forward neural network

The first ML model, forward neural network (*f-NN*), used to predict the total energy has two hidden layers with a size of 16 neurons each, where the Scaled Exponential Linear Unit (SeLU) activation function was applied after each hidden layer (see Supplementary Materials). The loss function for the *f-NN* is defined as below (L2-norm),

$$Loss = \sqrt{\sum_{r=1}^{N} \left(y_r - \check{y}_r\right)^2} \tag{5}$$

where N is the number of data, $\check{y}_r$ and y_r are the predictions and ground truths for the target. In Fig. 3, we illustrate the schematic of the *f-NN* energy model to predict the total energy of the atomic structure and the atomic configuration of FCC Ni-V alloy. With given atomic coordinates and types of the atomic element, the DFT calculation within MC simulation gives total energy with high computational time. In the *f-NN* energy model, atomic coordinates ($\vec{x}_1$, $\vec{x}_2$, $\vec{x}_3$) and atomic species in each coordinate are input features, and total energy is the output of the *f-NN* energy model. A total of 2,125 data include random, intermediate, and SRO configurations, which are quantitatively determined by the WC parameters. Table 1 has optimal forward network parameters obtained from a hyperparametric study minimizing testing error.

2.3.2. Inverse neural network

As the second ML model, inverse neural network (*i-NN*) used to predict the atomic configuration has two hidden layers with a size of 256 neurons each, where the Rectified Linear Unit (ReLU) activation function was applied after each hidden layer (see Supplementary Materials). The loss function for the *i-NN* is defined as below (binary cross-entropy),

$$Loss = -\frac{1}{N}\sum_{r=1}^{N}\left[y_r \log \check{y}_r + (1-y_r)\log\left(1-\check{y}_r\right)\right] \tag{6}$$

For the *i-NN* model, the ground truth y_r of data is labeled 1 or 0 as Ni or V atom. Using the *f-NN* based MC simulations, we generated a total of 2,125 configurations (atomic species and coordinates), with the SRO parameters calculated using Eq. (2). In the *i-NN* model, these SRO parameters are used as features. For the validation of the model, the SRO parameters used as features can be compared to those recalculated from the reconstructed coordinates (section 3.4), or the atomic species and coordinates can be directly (Supplementary Materials). In Fig. 4, we illustrate the schematic of the *i-NN* model to predict atomic structures for arbitrary SRO parameters. The input layer considers the average pair-wise SRO parameters from the three neighboring shells, while the output of the model is the atomic structure ($\vec{x}_1$, $\vec{x}_2$, $\vec{x}_3$, and species). A total of 2,125 data points used for the *f-NN* energy model are also employed to train the *i-NN* model. For simplicity of model, we fixed lattice coordinates for all atomic configurations and varied only atomic species in the output labels. Then the *i-NN* model is reduced to a simple binary classification. Once the *i-NN* model is validated, the arbitrary atomic configurations can be generated by directly specifying the desired SRO values. These configurations are then used to predict the CRSS levels, as described in section 3.5.

Similar to the *f-NN* model shown in section 2.3.1, Table 2 has listed *i-NN* model parameters obtained from hyperparametric study minimizing

Table 1
Optimal Hyperparameters Used in Forward Neural Network.

Hyper-Parameter	Optimizer	Activation Function,f	Learning Rate,β	Number of Hidden Layers	Neurons / Hidden Layer
Value	Adam	SeLU	1.00E-05	2	[16, 16]

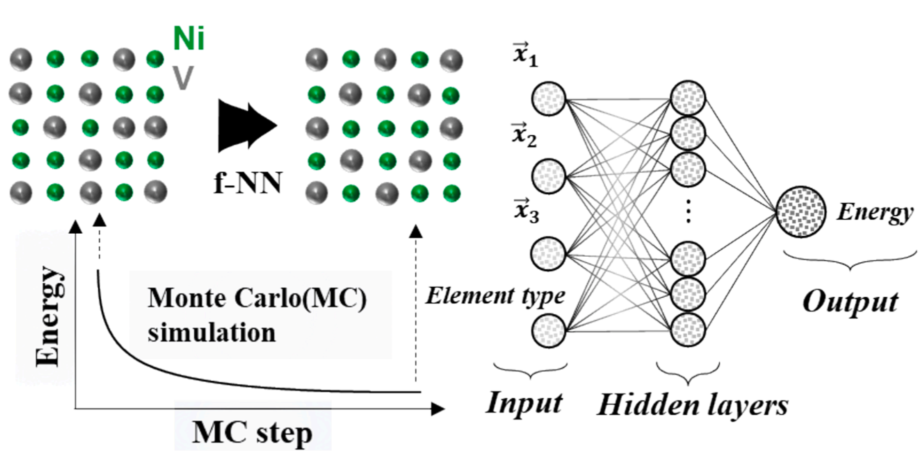

Fig. 3. Schematic of forward neural network (*f-NN*) energy model to predict total energy of atomic structure; Data is achieved from massive density functional theory (DFT) calculation within Monte Carlo (MC) simulation of swapping atomic species; Atomic coordinates ($\vec{x}_1$, $\vec{x}_2$, $\vec{x}_3$) and atomic species in each coordinate are input features, and total energy is the output of *f-NN* energy model; Atomic structures may include short-range order (SRO); The first nearest neighbor shell is defined in the figure with bonding from the center Ni atom.

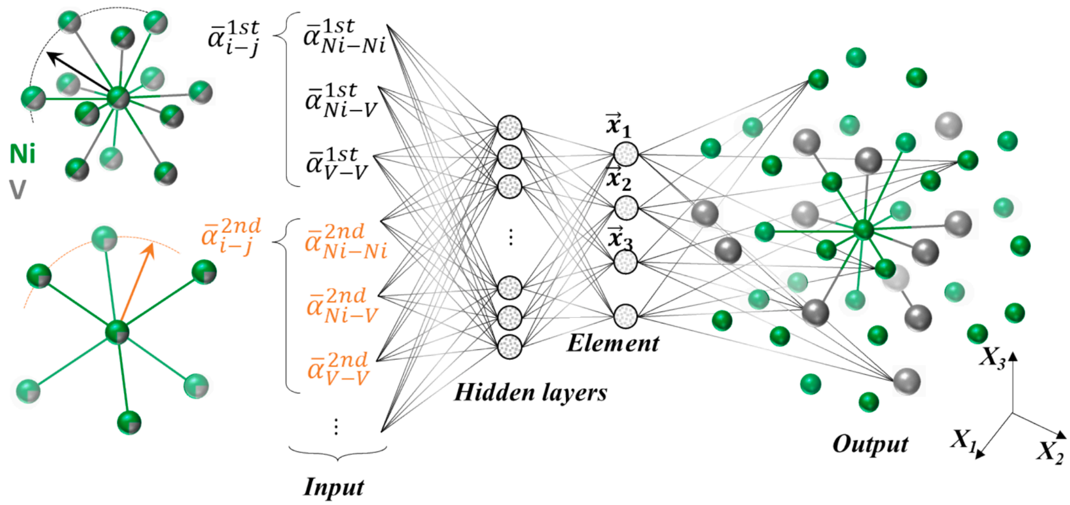

Fig. 4. Schematic of inverse neural network (*i-NN*) model to predict atomic structure for arbitrary short-range order (SRO); The DFT data used in *f-NN* energy model is also utilized for training *i-NN* model; SROs in different pairs (Ni-Ni, Ni-V, and V-V) for the first, second, and third nearest neighbor shells are input features, and atomic structure is output of *i-NN* model; For simplicity, only atomic species can be decoded into output label within fixed lattice coordinates.

Table 2
Optimal Hyperparameters Used in Inverse Neural Network.

Hyper-Parameter	Optimizer	Activation Function,f	Learning Rate,β	Number of Hidden Layers	Neurons / Hidden Layer
Value	Adam	ReLU	1.00E-03	2	[128, 256]

testing error. It is noticeable that the inverse problem has more complex functional dependencies that require a deeper network to yield optimal predictions.

3. Results

3.1. Total energy of atomic configuration

In Fig. 5, the result of *f-NN* energy model is provided. In Fig. 5**a**, total energies in a wide range composition of Ni-V alloys from the *f-NN* energy model agree well with the DFT calculations. In the Supplementary Materials, we plot the loss function upon the training process in 10,000 epochs in Fig. S1. The *f-NN* energy model reproduces high accuracies to predict the total energy with instant accessibility. The prediction resolution of the *f-NN* energy model can cover a small to a wide range of alloy compositions. In Fig. 5**b**, the comparison of total energy between the DFT and *f-NN* energy model in the example of a small composition range ($Ni_{70}V_{30}$) is depicted. As a demonstration of efficacy of the *f-NN* model, its instant accessibility to total energy during the MC simulation is presented in the next section.

3.2. Accelerating Monte Carlo simulation

In Fig. 6, we demonstrated the *f-NN* energy model to accelerate the MC simulation. Using the trained *f-NN* model, we replaced the MC simulation with the *f-NN* model to calculate total energy. After the onset of the *f-NN* model applied, the total energies of all compositions in this study converge within 500 MC steps. A total of ~ 490 MC steps take only instantaneous time (few milliseconds) for all compositions, which is considerably faster than the conventional DFT-MC simulation (~ 40 min

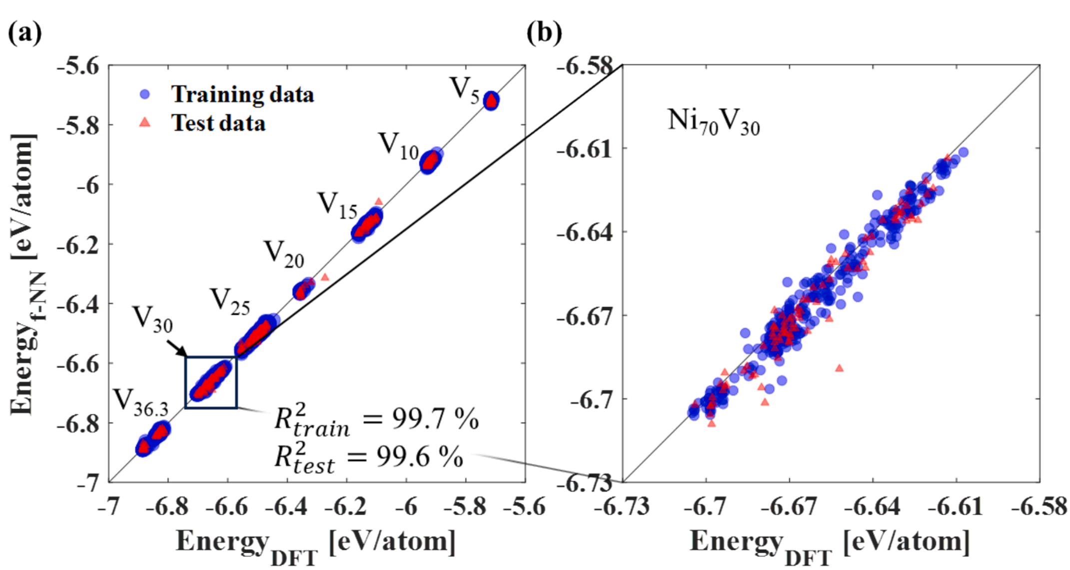

Fig. 5. Forward energy prediction – Result of the *f-NN* energy model; Comparison of ground truth (GT) energy based on the DFT and the predictions via the *f-NN* for (a) wide range of Ni-V compositions, (b) the example of small composition range in $Ni_{70}V_{30}$.

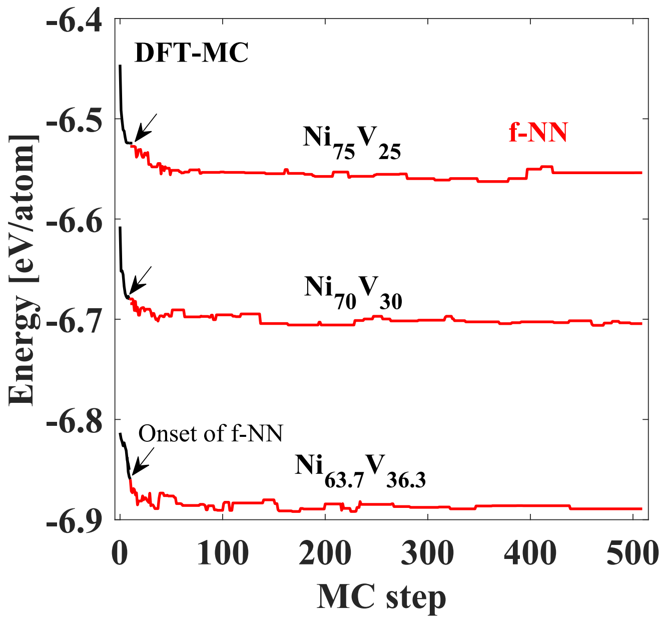

Fig. 6. Accelerated MC simulation via *f-NN* energy model; Quasi-random structures are initially set up; the MC simulation is implemented by DFT in only 10 steps, and then switched to the *f-NN* energy model to achieve energetically stable configurations.

per step). As the atomic configurations are stabilized further, the DFT-MC approach become increasingly time-consuming due to high number of rejected configurations. In contrast, by properly applying the *f-NN* model after a few steps of the MC simulation, a stabilized structure is obtained much more quickly. We utilized the stabilized atomic configurations obtained with the *f-NN* model for further analysis and the inverse design of SRO configurations.

3.3. Short-range order (SRO) of configuration

In Fig. 7**a**, we plot the SRO parameters upon the MC simulation. Eq. (2) gives the SRO parameters in each atomic pair for a single center atom. For the SRO characterization of the given crystal, the average over total number of atoms is conventionally used. The average SRO is defined as follows,

$$\overline{\alpha}^{m}_{i-j} = \frac{1}{n_{i-j}}\sum\nolimits_{k=1}^{n_{i-j}} \alpha^{m}_{i-j,k} \tag{7}$$

where n_{i-j} is total number of atoms for $i-j$ pairs, and $\alpha^{m}_{i-j,k}$ is the SRO at k-th site of center atomic species i. For $Ni_{63.7}V_{36.3}$ alloy composition (Ni: 172, V: 98), we have 172 Ni-Ni pairs, 270 Ni-V pairs, and 98 V-V pairs, respectively. As $Ni_{63.7}V_{36.3}$ alloy is being energetically stabilized, the SRO is converged, and the Ni-V pair (−) becomes more favorable than the Ni-Ni and V-V pairs (+) in the first neighbor shell. These average SRO parameters in each pair are utilized in the *i-NN* model in the next section.

In order to investigate the correlation between the overall level of SRO and total energy, we put the summation of each pair SRO parameter, defined as below,

$$\sum \overline{\alpha}^{m}_{i-j} = \sum\nolimits_{pair\,i-j} \overline{\alpha}^{m}_{i-j} \tag{8}$$

In Fig. 7**b**, the total average SRO parameters ($\sum \overline{\alpha}^{m}_{i-j}$) and total energy are compared for different alloy compositions. As the composition increases, the range of SRO parameters gets narrower since the solute atom has a low number of sites to swap from the initial position. Also, the summation parameter $\sum \overline{\alpha}^{m}_{i-j}$ represents always positive (see the Supplementary Materials) during the order treatment such as the MC simulation, no matter which composition of Ni-V alloy is given. Since $\sum \overline{\alpha}^{m}_{i-j}$ has one sign in positive, it is suitable to describe the overall level of SRO and total energy.

3.4. Inverse design of SRO

In Fig. 8, the result of the *i-NN* model is provided. In Fig. 8**a-b**, the SRO parameters (Ni-Ni and Ni-V pairs) used in the input features and calculated in the reconstructed configuration from the *i-NN* model are compared. The SRO parameters in a wide range composition of Ni-V alloys from the *i-NN* model agree well with the ground truths based on the MC simulation. In the Supplementary Materials, we provide the confusion matrix in Fig. S2 based on the number of sites with correctly predicted element. The *i-NN* model reproduces high accuracies to reconstruct the atomic configuration with only average SRO parameters. In Fig. 9, we compare the SRO of V-V pair and the weighted average SRO parameters based on the interaction energy, U_{i-j}. The introduction of interaction energy to the SRO was suggested by Flinn (Flinn, 1958), and Cohen and Fine (Cohen and Fine, 1962). As U_{i-j} is combined with the change of SRO upon slip, the CRSS and stacking fault energy can be also

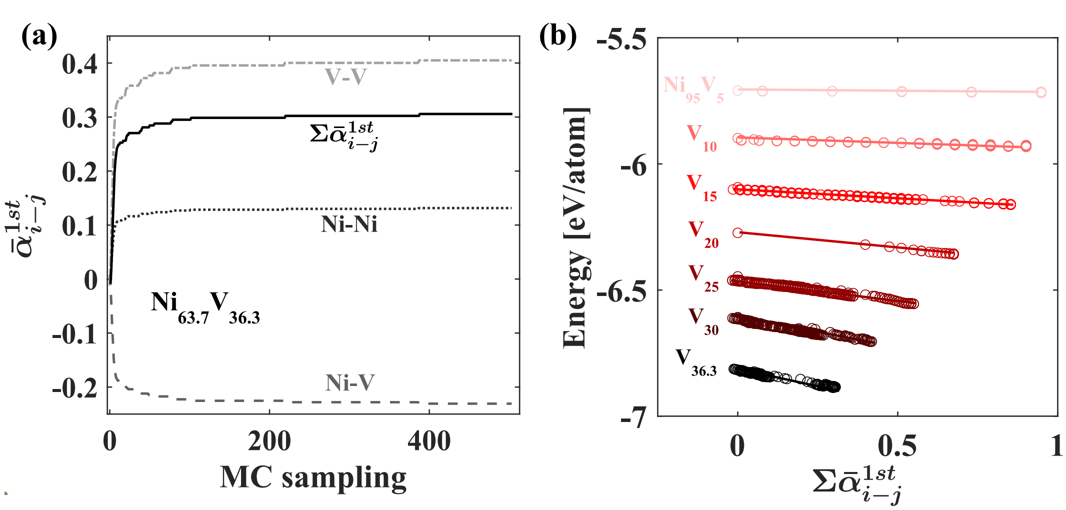

Fig. 7. Short-range order (SRO) characterization within the MC simulation; (a) SRO parameters defined in the first nearest neighbor shell for $Ni_{63.7}V_{36.3}$ composition; (b) Composition-dependent correlation between the SRO and cohesive energy.

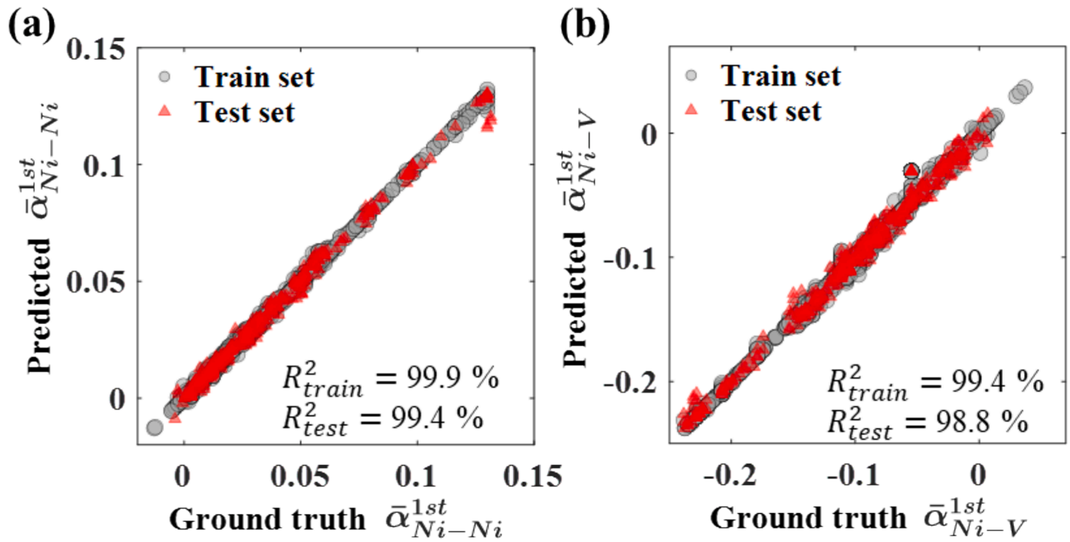

Fig. 8. Comparison of SRO parameters between ground truth values and predictions derived from reconstructed atomic structures using the *i-NN* model; (a) Ni-Ni, (b) Ni-V pairs.

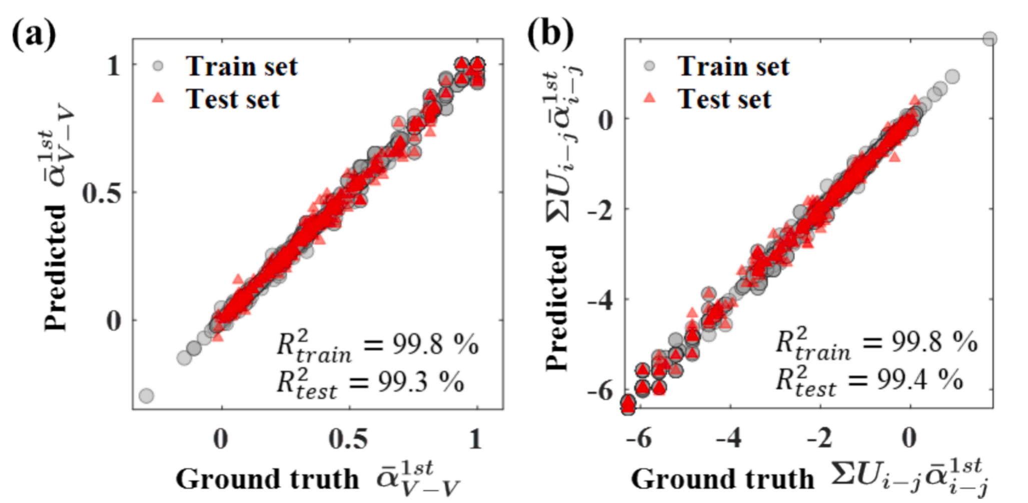

Fig. 9. Comparison of SRO parameters between ground truth values and predictions derived from reconstructed atomic structures using the *i-NN* model; (a) V-V pair, (d) interaction energy weighted summation $\sum_{i-j} U_{i-j}\bar{\alpha}^{m}_{i-j}$, where U_{i-j} is interaction energy between i and j atomic species.

predictable as shown in the previous work (You et al., 2024). Its demonstration on the CRSS is represented in the next section. The interaction term of each pair is obtained as $U_{Ni-Ni} = -4.21$ eV, $U_{Ni-V} = -7.20$ eV, and $U_{V-V} = -9.85$ eV in the DFT. The weighted summation $\sum U_{i-j}\bar{\alpha}^{1st}_{i-j}$ offers also good agreement for the *i-NN* model.

4. Prediction of CRSS

In this section, we show the application of the trained *i-NN* models to predict the CRSS. For the simplicity of the model with other properties, we utilize the recent CRSS theory (Celebi et al., 2024; Celebi et al., 2023; Mohammed et al., 2022; You et al., 2023a; You et al., 2023b). It takes into account "SRO change" in the Wigner-Seitz (WS) cell during slip motion, which dictates the CRSS and intrinsic stacking fault energy (γ_{isf}) (You et al., 2024). Therefore, we apply a slip in the reconstructed atomic configuration from the *i-NN* model and then estimate the CRSS by using the theory.

In Fig. 10, we illustrate the change of the SRO parameter during slip motion. We demonstrate the SRO change for a single Ni atom sampled from the superlattice of $Ni_{63.7}V_{36.3}$ alloy, and the first neighbor shell is defined with the WS cell during the slip. In the calculation of the SRO parameter, the host Ni atom in $Layer_0$ is considered as the center atom. Two layers ($Layer_{+1}$, $Layer_{-1}$) are overlaid together, as shown in the figure. The initial coordination number becomes 12, and the number of Ni-V pairs is 7. After the slip displacement, the V atom in the initial 12-th site of $Layer_{-1}$ is outside the WS cell, and its bond to the center Ni is broken in the first shell based on the WS cell definition. Then, the number of Ni-V pairs are changed to 6. This significantly contributes to the SRO value. At the intrinsic stacking fault (ISF) states, the new Ni atom in $Layer_{-1}$ is included in the WS cell as the new 12-th site ('12′), so its bond to the center Ni is restored. Two states (initial, ISF) have distinctive SRO values (−0.607, −0.378) by using nominal composition. We utilize this definition for different slip-planes by applying local concentrations of substitutional solute atoms. The concentration c_j in Eq. (2) can be substituted with the local compositions (such as two layer composition on $Layer_{(-1,0)}$). Then, we apply the correlation of SRO parameters with the SFEs and CRSS to estimate the CRSS of the reconstructed configuration from the *i-NN* model. Details of CRSS theory are described in the Supplementary Materials.

In Fig. 11**a**, we plot the data distributions of ground truth atomic

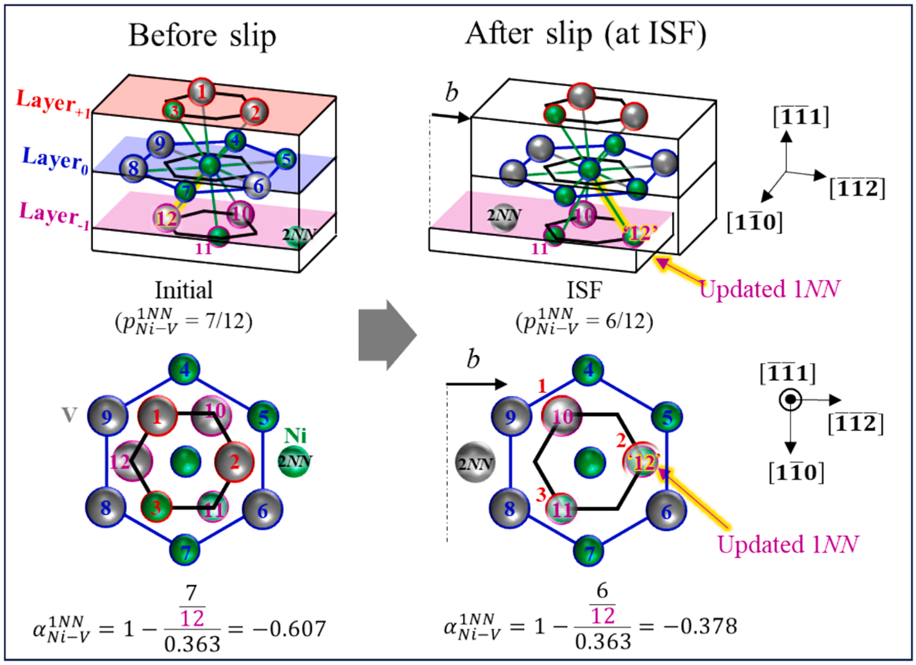

Fig. 10. Schematic of "short-range order (SRO) change" during slip motion; Total 3-layers illustrate a center layer ($Layer_0$; blue) and two layers ($Layer_{+1}$, $Layer_{-1}$) upper and below $Layer_0$. Color-outlines of atoms correspond to their layer colors. Probability (p^m_{i-j}) and SRO (α^m_{i-j}) of Ni-V pair are changed upon slip for center Ni atom; Ni and V atoms are colored green and grey; The Wigner-Seitz (WS) cell is represented as black hexagon. {111} plane view is shown at the bottom figures. $Layer_{+1}$ consists of atomic sites (1, 2, 3), $Layer_0$ (4, 5, 6, 7, 8, 9), and $Layer_{-1}$ (10, 11, 12), respectively.

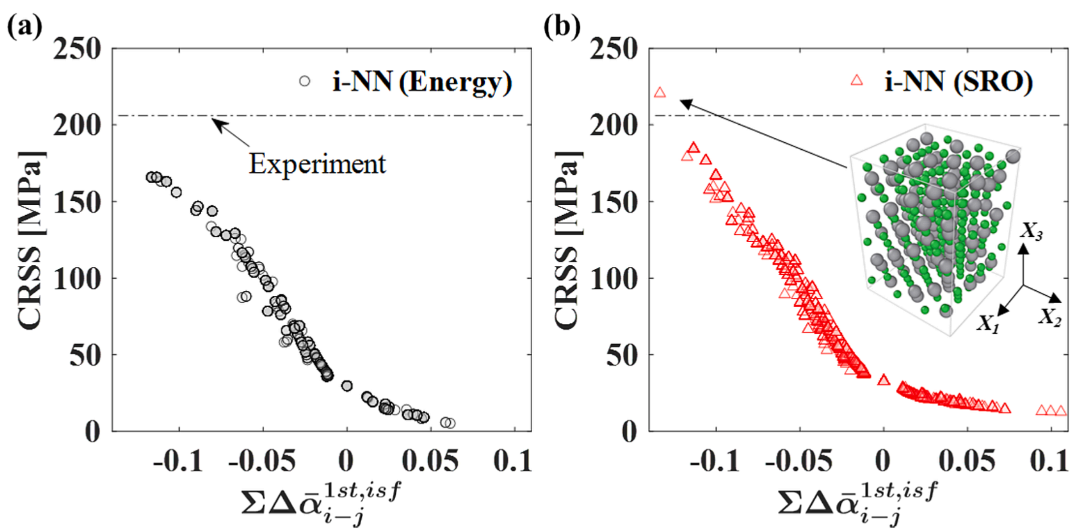

Fig. 11. Change of SRO and CRSS estimation $Ni_{63.7}V_{36.3}$ alloy. (a) The direct DFT-based calculation of atomic configurations is shown together with the inverse NN model-based ones. A total of ~ 1500 atomic configurations in $Ni_{63.7}V_{36.3}$ composition are reconstructed. (b) CRSS theory is applied to the reconstructed configurations by applying slip.

configurations ($Ni_{63.7}V_{36.3}$ composition) with the DFT-based MC simulations and the reconstructed configurations from the inverse NN model. The later configurations are reproduced in an instant time without the DFT and MC. The data distribution is based on the "SRO change" of $Ni_{63.7}V_{36.3}$ alloy by applying the weighted average with the interaction energy. A total of 2000 atomic configurations in $Ni_{63.7}V_{36.3}$ composition are reconstructed. In Fig. 11**b**, the CRSS theory is applied to the reconstructed configurations by applying slip. The largely negative $\Delta\bar{\alpha}^{1NN,isf}_{sum}$ corresponds to higher CRSS and γ_{isf}, while the positive $\Delta\bar{\alpha}^{1NN,isf}_{sum}$ can even yield less than 10 MPa. The positive $\Delta\bar{\alpha}^{1NN,isf}_{sum}$, however, is not physically preferred in short-range ordered materials, whereas chemically random configuration may have the positive $\sum\Delta\bar{\alpha}^{1st,isf}_{i-j}$. The negative $\Delta\bar{\alpha}^{1NN,isf}_{sum}$ is statistically preferred, and it would result in the higher CRSS and γ_{isf}. Also, the highest stress barrier should be overcome in the macroscale deformation, which is confirmed in the experiment of the previous study.

5. Discussion of results

In this study, we established an ML approach to construct models that can predict atomic configuration as well as material properties such as total energy and CRSS. These models hold considerable significance in this field due to their potential to streamline material design processes. For instance, the *f-NN* energy model allows for instant estimation ($t_{cpu} \sim 1$ ms) of total energy for the given atomic configuration, in contrast to the standard DFT-based MC simulation, which typically necessitates approximately 40 min per step. Furthermore, our model training approach exhibits noteworthy efficiency, Although the inclusion of training data for novel material systems may initially impose additional time requirements, this overhead diminishes progressively with ongoing training iterations.

In the context of the *i-NN* model and its results, the primary objective is to predict atomic configurations, enabling it solely based on the given total energy or the SRO parameters without implementing the MC simulations. As shown in Fig. 11, the CRSS predictions derived from the *i-NN* based atomic configurations exhibit a broader spectrum of values compared to those predicted using the DFT-MC-based atomic configurations in a recent paper (You et al., 2024). This implies that CRSS ranges, which cannot be captured through the DFT-MC simulations due to their demanding computational time, can be readily identified utilizing the ML model. With an additional amount of data from a novel material system, it appears feasible to predict the CRSS within the unknown compositional region of the system.

To construct Fig. 10, multiple slip-cuts were considered, which corresponded to different γ_{isf} and "SRO change" on the Wigner-Seitz lattice. This is the uniqueness of our approach to CRSS determination, which is enriched by the inverse neural network methodology presented in this paper. The local compositional changes affect both SRO and γ_{isf}. Indeed, the local distortions due to different atomic radii and electron density are reflected in γ_{us} and γ_{isf} calculations which are key inputs to the framework.

In the CRSS predictions based on the *i-NN* depicted in Fig. 11, it is evident that utilizing the SRO parameters as variables that yield predictions closer to the experimental CRSS compared to when total energy is only employed. This observation suggests that total energy alone may not adequately represent the CRSS in terms of atomic configuration, as compared to the SRO parameters. This is because there could be multiple atomic configurations that exhibit similar energy levels, but their local short-range order is significantly different. Also, the "SRO change" in those pertinent arrangements can be different, and it exerts a substantial influence on the CRSS. Hence, it is worthwhile to identify the SRO parameters in experiments for accurate predictions of initial atomic configuration in order to obtain the CRSS, as our *i-NN* model suggests.

Finally, the SRO parameters for the *i-NN* model were defined in the first, second, and third nearest neighbor shells ($\overline{\alpha}^{1st}_{i-j}$, $\overline{\alpha}^{2nd}_{i-j}$, $\overline{\alpha}^{3rd}_{i-j}$), and these variables were utilized to reconstruct atomic configurations. For the estimate of CRSS, however, the "SRO change" induced by slip advance in the first nearest neighbor shell ($\Delta\overline{\alpha}^{1st}_{i-j}$) shows a sufficient measurer, as detailed in the previous work (You et al., 2024). Then, the CRSS is dictated by the negatively large "SRO change" at the intrinsic stacking fault point ($\Delta\overline{\alpha}^{1st,isf}_{i-j}$), directly linked to the γ_{isf}. By summing up these parameters with the provided interaction energy (U_{i-j}), the γ_{isf} becomes readily predictable on average. In essence, rather than precisely determining the γ_{isf} with heavy DFT calculations, a prediction sufficiently close to the experimental CRSS can be achieved by using "SRO change." We encourage the readers to simply use the ML models as well as the "SRO change" concept further to investigate other material systems.

CRediT authorship contribution statement

Daegun You: Software, Methodology, Conceptualization, Data curation, Formal analysis, Investigation, Validation, Visualization, Writing – original draft, Writing – review & editing. **Orcun Koray Celebi:** Methodology, Investigation, Writing – original draft, Writing – review & editing. **Diab W. Abueidda:** Software, Methodology, Conceptualization, Investigation, Writing – original draft, Writing – review & editing. **Gorkem Gengor:** Investigation, Methodology, Software. **Ahmed Sameer Khan Mohammed:** Methodology, Conceptualization, Investigation, Software, Supervision. **Seid Koric:** Writing – review & editing, Investigation, Conceptualization, Project administration, Resources, Supervision. **Huseyin Sehitoglu:** Writing – review & editing, Funding acquisition, Conceptualization, Project administration, Resources, Supervision.

Declaration of competing interest

The authors declare that they have no known competing financial interests or personal relationships that could have appeared to influence the work reported in this paper.

Acknowledgment

The work is supported by the National Science Foundation (NSF) under award number CMMI-21–25821, which is gratefully acknowledged. This research was also supported in part by the Illinois Computes project which is supported by the University of Illinois Urbana-Champaign and the University of Illinois System. This research used the Delta advanced computing and data resource which is supported by the National Science Foundation (award OAC 2005572) and the State of Illinois. Delta is a joint effort of the University of Illinois Urbana-Champaign and its National Center for Supercomputing Applications (NCSA). The authors would also like to thank NCSA at the University of Illinois, particularly its Research Consulting Directorate, the Center for Artificial Intelligence Innovation (CAII), and the Illinois Campus Cluster Program (ICCP) for their support.

Appendix A. Supplementary data

Supplementary data to this article can be found online at https://doi.org/10.1016/j.ijsolstr.2024.113175.

Data availability

Data will be made available on request.

References

Abueidda, D.W., Koric, S., Sobh, N.A., Sehitoglu, H., 2021. Deep learning for plasticity and thermo-viscoplasticity. Int. J. Plast 136, 102852.
Abuzaid, W., Sehitoglu, H., 2017. Critical resolved shear stress for slip and twin nucleation in single crystalline FeNiCoCrMn high entropy alloy. Mater. Charact. 129, 288–299.
Argon, A., 2007. Strengthening mechanisms in crystal plasticity. OUP Oxford.
Asaro, R., Lubarda, V., 2006. Mechanics of solids and materials. Cambridge University Press.
Barry, M.C., Gissinger, J.R., Chandross, M., Wise, K.E., Kalidindi, S.R., Kumar, S., 2023. Voxelized atomic structure framework for materials design and discovery. Comput. Mater. Sci 230, 112431.
Celebi, O.K., Mohammed, A.S.K., Sehitoglu, H., 2023. Effect of Dislocation Character on the CRSS. Acta Mater. 254, 118982.
Celebi, O.K., Gengor, G., You, D., Mohammed, A.S.K., Bucsek, A., Sehitoglu, H., 2024. Distorted dislocation cores and asymmetric glide resistances in titanium. Acta Mater. 274, 119967.
Chen, S., Aitken, Z.H., Pattamatta, S., Wu, Z., Yu, Z.G., Srolovitz, D.J., Liaw, P.K., Zhang, Y.-W., 2021a. Simultaneously enhancing the ultimate strength and ductility of high-entropy alloys via short-range ordering. Nat. Commun. 12, 4953.
Chen, X., Wang, Q., Cheng, Z., Zhu, M., Zhou, H., Jiang, P., Zhou, L., Xue, Q., Yuan, F., Zhu, J., Wu, X., Ma, E., 2021b. Direct observation of chemical short-range order in a medium-entropy alloy. Nature 592, 712–716.
Cohen, J.B., Fine, M.E., 1962. Some aspects of short-range order. J. Phys. Radium 23, 749–762.
Cowley, J.M., 1960. Short- and Long-Range Order Parameters in Disordered Solid Solutions. Phys. Rev. 120, 1648–1657.
Ding, J., Yu, Q., Asta, M., Ritchie, R.O., 2018. Tunable stacking fault energies by tailoring local chemical order in CrCoNi medium-entropy alloys. Proc. Natl. Acad. Sci. 115, 8919–8924.
Ferrari, A., Körmann, F., Asta, M., Neugebauer, J., 2023. Simulating short-range order in compositionally complex materials. Nat. Comput. Sci. 3, 221–229.

Flinn, P.A., 1958. Solute hardening of close-packed solid solutions. Acta Metall. 6, 631–635.
Goodfellow, I., 2016. Deep learning. MIT press.
Hastings, W.K., 1970. Monte Carlo sampling methods using Markov chains and their applications. Biometrika 57, 97–109.
Kollmann, H.T., Abueidda, D.W., Koric, S., Guleryuz, E., Sobh, N.A., 2020. Deep learning for topology optimization of 2D metamaterials. Mater. Des. 196, 109098.
Kresse, G., Furthmüller, J., 1996. Efficient iterative schemes for ab initio total-energy calculations using a plane-wave basis set. Phys. Rev. B 54, 11169–11186.
Kresse, G., Joubert, D., 1999. From ultrasoft pseudopotentials to the projector augmented-wave method. Phys. Rev. B 59, 1758–1775.
Li, Q.-J., Sheng, H., Ma, E., 2019. Strengthening in multi-principal element alloys with local-chemical-order roughened dislocation pathways. Nat. Commun. 10, 3563.
Li, Y., Wei, Y., Wang, Z., Liu, X., Colnaghi, T., Han, L., Rao, Z., Zhou, X., Huber, L., Dsouza, R., Gong, Y., Neugebauer, J., Marek, A., Rampp, M., Bauer, S., Li, H., Baker, I., Stephenson, L.T., Gault, B., 2023. Quantitative three-dimensional imaging of chemical short-range order via machine learning enhanced atom probe tomography. Nat. Commun. 14, 7410.
Marceau, R.K.W., Ceguerra, A.V., Breen, A.J., Palm, M., Stein, F., Ringer, S.P., Raabe, D., 2015a. Atom probe tomography investigation of heterogeneous short-range ordering in the 'komplex' phase state (K-state) of Fe–18Al (at.%). Intermetallics 64, 23–31.
Marceau, R.K.W., Ceguerra, A.V., Breen, A.J., Raabe, D., Ringer, S.P., 2015b. Quantitative chemical-structure evaluation using atom probe tomography: Short-range order analysis of Fe–Al. Ultramicroscopy 157, 12–20.
Mohammed, A.S.K., Celebi, O.K., Sehitoglu, H., 2022. Critical stress prediction upon accurate dislocation core description. Acta Mater. 233, 117989.
Muhammad, W., Brahme, A.P., Ibragimova, O., Kang, J., Inal, K., 2021. A machine learning framework to predict local strain distribution and the evolution of plastic anisotropy & fracture in additively manufactured alloys. Int. J. Plast 136, 102867.
Nabarro, F.R.N., 1947. Dislocations in a simple cubic lattice. Proc. Phys. Soc. 59, 256–272.
Niu, C., LaRosa, C.R., Miao, J., Mills, M.J., Ghazisaeidi, M., 2018. Magnetically-driven phase transformation strengthening in high entropy alloys. Nat. Commun. 9, 1363.
Norman, N., Warren, B.E., 2004. X-Ray Measurement of Short Range Order in Ag-Au. J. Appl. Phys. 22, 483–486.
Pattanayak, S., Pattanayak, J.S., John, S., 2017. Pro deep learning with tensorflow. Springer.
Peierls, R., 1940. The size of a dislocation. Proc. Phys. Soc. 52, 34.
Perdew, J.P., Burke, K., Ernzerhof, M., 1996. Generalized Gradient Approximation Made Simple. Phys. Rev. Lett. 77, 3865–3868.
Picak, S., Singh, P., Salas, D., Tunes, M.A., Fang, X., Zhou, L., Kramer, M.J., Chumlyakov, Y.I., Johnson, D.D., Arroyave, R., Ren, Y., Karaman, I., 2023. Orientation dependence of the effect of short-range ordering on the plastic deformation of a medium entropy alloy. Mater. Sci. Eng. A 888, 145309.
Pradeep, K.G., Wanderka, N., Choi, P., Banhart, J., Murty, B.S., Raabe, D., 2013. Atomic-scale compositional characterization of a nanocrystalline AlCrCuFeNiZn high-entropy alloy using atom probe tomography. Acta Mater. 61, 4696–4706.
Salmenjoki, H., Alava, M.J., Laurson, L., 2018. Machine learning plastic deformation of crystals. Nat. Commun. 9, 5307.
Santos-Florez, P.A., Dai, S.-C., Yao, Y., Yanxon, H., Li, L., Wang, Y.-J., Zhu, Q., Yu, X.-X., 2023. Short-range order and its impacts on the BCC MoNbTaW multi-principal element alloy by the machine-learning potential. Acta Mater. 255, 119041.
Schoeck, G., 1994. The generalized Peierls–Nabarro model. Philos. Mag. A 69, 1085–1095.
van de Walle, A., Tiwary, P., de Jong, M., Olmsted, D.L., Asta, M., Dick, A., Shin, D., Wang, Y., Chen, L.Q., Liu, Z.K., 2013. Efficient stochastic generation of special quasirandom structures. Calphad 42, 13–18.
Wang, X., Maresca, F., Cao, P., 2022. The hierarchical energy landscape of screw dislocation motion in refractory high-entropy alloys. Acta Mater. 234, 118022.
Widom, M., Huhn, W.P., Maiti, S., Steurer, W., 2014. Hybrid Monte Carlo/Molecular Dynamics Simulation of a Refractory Metal High Entropy Alloy. Metall. Mater. Trans. A 45, 196–200.
Yin, S., Zuo, Y., Abu-Odeh, A., Zheng, H., Li, X.-G., Ding, J., Ong, S.P., Asta, M., Ritchie, R.O., 2021. Atomistic simulations of dislocation mobility in refractory high-entropy alloys and the effect of chemical short-range order. Nat. Commun. 12, 4873.
You, D., Ganorkar, S., Kim, S., Kang, K., Shin, W.-Y., Lee, D., 2020. Machine learning-based prediction models for formation energies of interstitial atoms in HCP crystals. Scr. Mater. 183, 1–5.
You, D., Celebi, O.K., Mohammed, A.S.K., Abueidda, D.W., Koric, S., Sehitoglu, H., 2023a. CRSS determination combining ab-initio Framework and Surrogate Neural Networks. Int. J. Plast 103524.
You, D., Celebi, O.K., Mohammed, A.S.K., Sehitoglu, H., 2023b. Negative Stacking Fault Energy in FCC materials-Its Implications. Int. J. Plast 103770.
You, D., Celebi, O.K., Gengor, G., Mohammed, A.S.K., Abuzaid, W., Sehitoglu, H., 2024. Short-range ordering mechanics in FCC materials. Int. J. Plast 174, 103919.
Zhang, M., Yu, Q., Frey, C., Walsh, F., Payne, M.I., Kumar, P., Liu, D., Pollock, T.M., Asta, M.D., Ritchie, R.O., Minor, A.M., 2022. Determination of peak ordering in the CrCoNi medium-entropy alloy via nanoindentation. Acta Mater. 241, 118380.
Zhang, R., Zhao, S., Ophus, C., Deng, Y., Vachhani, S.J., Ozdol, B., Traylor, R., Bustillo, K. C., Morris, J.W., Chrzan, D.C., Asta, M., Minor, A.M., 2019. Direct imaging of short-range order and its impact on deformation in Ti-6Al. Sci. Adv. 5, eaax2799.
Zhang, R., Zhao, S., Ding, J., Chong, Y., Jia, T., Ophus, C., Asta, M., Ritchie, R.O., Minor, A.M., 2020. Short-range order and its impact on the CrCoNi medium-entropy alloy. Nature 581, 283–287.
Zhao, S., Stocks, G.M., Zhang, Y., 2017. Stacking fault energies of face-centered cubic concentrated solid solution alloys. Acta Mater. 134, 334–345.
Zhao, S., Osetsky, Y., Stocks, G.M., Zhang, Y., 2019. Local-environment dependence of stacking fault energies in concentrated solid-solution alloys. npj Comput. Mater. 5, 13.
Zhou, L., Wang, Q., Wang, J., Chen, X., Jiang, P., Zhou, H., Yuan, F., Wu, X., Cheng, Z., Ma, E., 2022. Atomic-scale evidence of chemical short-range order in CrCoNi medium-entropy alloy. Acta Mater. 224, 117490.